


CT reconstruction and MRI fusion of 3D rotational angiography in the evaluation of pediatric cerebrovascular lesions

Prakash Muthusami¹  · Nicholas Shkumat² · Vanessa Rea¹ · Albert H. Chiu³ · Manohar Shroff¹

Received: 18 January 2017 / Accepted: 6 March 2017 / Published online: 27 March 2017
© Springer-Verlag Berlin Heidelberg 2017

Abstract

Purpose Complex neurovascular lesions in children require precise anatomic understanding for treatment planning. Although 3DRA is commonly employed for volumetric reformation in neurointerventional procedures, the ability to reconstruct this data into CT-like images (3DRA-CT) is not widely utilized. This study demonstrates the feasibility and usefulness of 3DRA-CT and subsequent MRI fusion for problem solving in pediatric neuroangiography.

Methods This retrospective study includes 18 3DRA-CT studies in 16 children (age 9.6 ± 3.8 years, range 2–16 years) over 1 year. After biplane 2D-digital subtraction angiography (DSA), 5-second 3DRA was performed with selective vessel injection either with or without subtraction. Images were reconstructed into CT sections which were post-processed to generate multiplanar reformation (MPR) and maximum intensity projection (MIP) images. Fusion was performed with 3D T1 MRI images to precisely demonstrate neurovascular relationships. Quantitative radiation metrics were extracted and compared against those for the entire examination and for corresponding biplane 2D-DSA acquisitions.

Results In all 18 cases, the 3DRA procedure and MRI fusion were technically successful and provided clinically useful information relevant to management. The unsubtracted and subtracted 3DRA acquisitions were measured to deliver 5.9 and 132.2%, respectively, of the mean radiation dose of corresponding biplane 2D-DSA acquisitions and contributed 1.2 and 12.5%, respectively, to the total procedure dose.

Conclusion Lower radiation doses, high spatial resolution, and multiplanar reformatting capability make 3DRA-CT a useful adjunct to evaluate neurovascular lesions in children. Fusing 3DRA-CT data with MRI is an additional capability that can further enhance diagnostic information.

Keywords Cerebral angiography · Cone-beam computed tomography · Pediatric · Radiation dose · Three-dimensional imaging

Introduction

Cerebrovascular lesions in children are challenging to image due to limitations of resolution, contrast volume, and flow rates. Catheter angiography is required to answer specific questions in complex intracranial lesions including arteriovenous malformations (AVM), arteriovenous fistulae (AVF), and aneurysms. Multiple 2D projections are necessary for a complete assessment. Unfortunately, even with modern dose optimization paradigms, multiple acquisitions result in substantial radiation dose and increase the volume of contrast medium used. Given these challenges, this manuscript describes the use of CT reconstruction of 3D rotational angiographic acquisitions (3DRA) in pediatric neuroangiography, which has the potential to increase diagnostic confidence while decreasing the number of acquisitions required, and thereby, radiation dose.

✉ Prakash Muthusami
prakash.muthusami@sickkids.ca

¹ Pediatric Neuroradiology and Image Guided Therapy, Department of Diagnostic Imaging, The Hospital for Sick Children, 555 University Avenue, Toronto, ON M5G 1X8, Canada

² Medical Physics, Department of Diagnostic Imaging, The Hospital for Sick Children, Toronto, ON, Canada

³ Department of Interventional Neuroradiology, Institute of Neurological Sciences, Prince of Wales Hospital, Randwick, NSW, Australia

Cone beam CT (CBCT) has gained acceptance in the neurointerventional community as a useful tool for diagnosis, analysis, and treatment planning [1–4]. Some of the described applications include the assessment of luminal apposition of intracranial stents [5, 6] and for evaluating procedural complications like infarcts or subarachnoid hemorrhage [7, 8]. However, these protocols typically require long (20 s) acquisitions, leading to motion artifact and venous contamination during angiography [9], with radiation doses as high as conventional CT [10]. Of late, 3DRA with a rotational time of 5–10 s has been increasingly used for generating volume-rendered (VR) reformats for intracranial aneurysm treatment planning [11–13]. However, processing raw data from 3DRA into CT-like images is not widely utilized. This technique has several advantages over conventional CT angiography (CTA), including lower radiation and contrast doses as well as inherently high spatial resolution, which make it attractive for problem solving in pediatric neuroangiography. In addition, it lends itself to VR and MPR reformation similar to CTA, as well as fusion with previously performed MRI studies, thereby allowing precise angio-topographical correlations to be made.

Methods

Institutional approval was obtained for this retrospective study. For a 1-year period between October 2015 and September 2016, a total of 74 neuroangiographic procedures were performed in 58 children. Written informed consent was obtained from parents/guardians for all procedures. Of these examinations, 18 3DRA acquisitions had been performed in 16 patients. The indications for 3DRA-CT are shown in Table 1.

DSA protocol

All procedures were performed under general anesthesia in a biplane neurointerventional suite (Artis Q, Siemens Healthcare, Erlangen, Germany) by two pediatric neuroradiologists (M.S. and P.M.). Standard angiographic technique was used to catheterize the neck arteries with a 4Fr angiographic catheter via femoral arterial access, with systemic heparinization of 50–100 U/kg, except in the setting of acute hemorrhage. 2D-digital subtraction angiography (DSA) images were obtained with a 1024 × 1024 matrix, 32-cm field of view (FOV), and temporal resolution of 3–6 frames/s. Undiluted iodinated contrast (Iohexol 300 mg/ml, Ommipaque 300, GE Healthcare, Ontario, Canada) was injected through a power injector, with flow rates (ranging between 2.5 and 5 ml/s) and contrast volumes (ranging between 5 and 12 ml) chosen by the operators based on the size of the artery and catheter position. In smaller vessels, a rise time of 0.5–1 s was added.

A 5-s 3DRA was performed in the vessel (s) of interest using the same flat-panel detector system, FOV 42-cm, and acquisition matrix 1024 × 1024. The 3DRA protocol chosen was either subtracted or non-subtracted, depending on the pathology, type of information required, and method of post-processing preferred to depict the lesion. These protocols were customized by the interventional team in an effort to provide diagnostic image quality at a reasonably low radiation dose. Essential aspects of these acquisitions are briefly summarized in Table 2. Injections for 3DRA were performed through a power injector, maintaining the same flow rate used for 2D-DSA in that vessel, and adding a 1–2 s X-ray acquisition delay after the start of contrast injection. For subtracted 3DRA, full-strength contrast was injected to retain the ability to generate

Table 1 Patient demographic and indications (*N* = 16)

Parameter		Value
Age (mean ± SD in years)		9.6 ± 3.8
Male/female		11:5
General anesthesia (%)		100
Indications for 3DRA-CT (<i>N</i> = 18)	AVM nidus localization ^a	8
	AVM angioarchitecture ^b	3
	Aneurysm architecture	2
	Other	
	Suspected dissection flap	2
	Neurovascular anatomy delineation ^c	2
	Pial AVF	1

^a AVM nidus localization by fusion with MRI for residual/recurrent nidus posttreatment and for small nidus in anatomically challenging locations (e.g., in the fornix)

^b AVM architecture, including feeding arteries, flow-related and intranidal aneurysms/false aneurysms, and, if present, site of fistula with draining vein

^c Includes ascending pharyngeal artery to PICA connection (*n* = 1) and tortuous origin of ophthalmic artery during intra-arterial chemotherapy for retinoblastoma (*n* = 1)

Table 2 3D-rotational angiographic protocols employed and clinical situations wherein these would be preferred ($N = 18$)

5-s 3DRA protocol	Number	Projections (over 200 ⁰)	fps	Added filtration (mm Cu)	nGy/frame	Contrast concentration (%)	Clinical scenario(s), advantages, and disadvantages
Subtracted	11	133	30	0	360	100%	<ul style="list-style-type: none"> • Ideal for VR representation of a structural lesion (e.g., intracranial aneurysm) • Obtaining ideal working projection (e.g., prior to endovascular treatment of AVM or aneurysm) • For examining a lesion in multiple DSA projections (e.g., to assess nidal architecture, draining venous pattern of AVM) at various time phases after injection (i.e. 4D-DSA) • Radiation dose significantly higher than unsubtracted 3DRA and comparable to a biplane 2D-DSA acquisition • More manual inputs needed to co-register with MRI, due to subtraction of bone landmarks. Major arteries can be used for registration. However, unsubtracted CT can be retrospectively reconstructed to obtain bone landmarks for fusion • 3DRA-CT and fused image with MRI shows more streak artifact due to undiluted contrast
Unsubtracted	7	248	60	0.6	100	20–30%	<ul style="list-style-type: none"> • Ideal for small and deep AVMs, inadequately represented on 2D-DSA. These can be visualized on 3DRA-CT post-processed images • Excellent image quality of reconstructed 3DRA-CT images and fused images with MRI, with minimal to no streak artifact • Radiation dose significantly lower than subtracted 3DRA as well as 2D-DSA acquisitions • Easier automatic co-registration with MRI using bone and vascular landmarks • Unmasked 3DRA image with low-contrast concentration cannot be analyzed per se without reconstruction into 3DRA-CT • Difficult to obtain VR images due to reduced contrast concentration. Instead, excellent thick MIP images can be generated. However, vascular structures at skull base are harder to delineate

AVF arteriovenous fistula, AVM arteriovenous malformation, Cu copper, fps frames per second, MIP maximum intensity projection, VR volume reformatted

VR images. For unsubtracted 3DRA, contrast was diluted to 30% to reduce total contrast volume and streak artifact.

MRI imaging

MR imaging was performed either on a 1.5T magnet (Achieva, Philips Medical Systems, Best, The Netherlands) using an 8-channel head coil or on a 3T magnet (Achieva, Philips Medical Systems, Best, The Netherlands) using a 32-channel multi-transmit head coil. After acquiring three-plane scout localizers, sagittal 3D turbo field echo (TFE) T1 was performed (1.5T: TR/TE 9.8 ms/4.6 ms, flip angle 15⁰, FOV 22-cm, 1.0-mm isotropic voxels, bandwidth 150 Hz/pixel, parallel imaging factor 2, number of averages 1, acquisition time 6 min 30 s; 3T: TR/TE 4.9 ms/2.3 ms, flip angle 8⁰, FOV 22-cm, 1.0-mm isotropic voxels, bandwidth 394 Hz/pixel, parallel imaging factor 2, number of averages 1, acquisition time 4 min 20 s). Other sequences were performed as clinically required including time of flight MR angiography (1.5T: TR/TE 17.5 ms/4.5 ms, flip angle 20⁰, FOV 20-cm, slice thickness 1.2-mm, bandwidth 115 Hz/pixel, number of averages 2, acquisition time 7 min 10 s; 3T: TR/TE

25.0 ms/3.5 ms, flip angle 20⁰, FOV 20-cm, slice thickness 1.2-mm, bandwidth 217 Hz/pixel, number of averages 1, acquisition time 5 min 40 s) and post-contrast 3D-TFE T1 imaging, but these were not used for image registration and fusion for this study.

Image post-processing and 3DRA-MRI fusion

Image post-processing and fusion was performed by an experienced interventional radiology technologist and monitored by a neuroradiologist. 3DRA images were post-processed at the accompanying workstation using a 512 × 512 × 512 image matrix and appropriate kernel to create a 3DRA-CT volume with isotropic voxels. Axial, sagittal, and coronal images of the region of interest were created in addition to multiplanar reconstruction (MPR) and maximum intensity projection (MIP) images as required to best delineate the structures of interest. For subtracted acquisitions, VR images were generated in addition. A 3D fusion program (Syngo fusion package, Siemens Healthcare, Erlangen, Germany) on the same workstation was used to integrate reconstructed 3DRA-CT volumes with the previously acquired pre-contrast 3D-T1WI

MRI sequence. The underlying principles of the 2D-3D registration have been described elsewhere [14]. Image alignment prior to registration and fusion was performed as an automated or semi-automated function, using bony landmarks when present (orbit, sella, odontoid process) in three planes or the spatial overlap of intracranial arteries (supraclinoid carotid artery, basilar artery) when bones were subtracted. The resultant ‘fused’ image was post-processed using MPR and MIP reformats to depict the relevant lesion and its neuroanatomical relationships. Thin slices (1 mm MPR images with 1 mm gap) as well as thick slabs (10–20 mm MIP images) were generated in axial, sagittal, and coronal planes. The time taken for image post-processing and MRI fusion was 5–10 min.

Dosimetric analysis

Quantitative radiation dose surrogates including air kerma-area product (P_{KA}) and reference point air kerma ($K_{a,r}$) were extracted from radiation dose-structured reports. Each instance of radiation (fluoroscopy, fluorography, and rotational acquisition) was evaluated as a metric for patient dose. 3DRA data was separated into two categories (subtracted and unsubtracted protocols) based on technical factors. For each procedure, the contribution of the 3DRA acquisition to the total procedural radiation dose was reported as a percentage. In addition, radiation output from 3DRA acquisition was compared with that from biplane acquisitions in the same artery in two ways: (1) with radiation dose of the entire biplane acquisition, which was acquired for clinical information, and (2) with the dose of the biplane acquisition, normalized to a standardized duration (10-s, similar to the acquisition time for a subtracted 5-s 3DRA examination). With regard to clinical image quality and efficacy of 3DRA-CT and MRI fusion, the value in depicting angioarchitecture and the relationship to adjacent structures was qualitatively assessed.

Results

A total of 18 3DRA examinations had been performed in 16 children. The mean age was 9.6 ± 3.8 years (range 2–16 years). 3DRA with subtraction (using full strength contrast) was performed in 11 children, and without subtraction (using 30% contrast) in 7. All procedures were technically successful with diagnostic image quality with no artifacts impeding post-processing and visualization. MRI fusion was performed semi-automatically in all cases.

The mean $K_{a,r}$ and P_{KA} were 46.5 mGy and 10.2 Gy cm² for subtracted 3DRA acquisitions and 2.6 mGy and 0.63 Gy cm² for unsubtracted 3DRA acquisitions, respectively. When compared to biplane 2D-DSA, the $K_{a,r}$ proportion ranged from 51.7 to 309.5% for subtracted 3DRA and only 3.3–11.7% for the unsubtracted 3DRA protocols. The radiation dose of unsubtracted 3DRA was significantly lower than that of subtracted 3DRA ($p < 0.0001$) and that of corresponding 2D-DSA ($p = 0.001$). The radiation dose of subtracted 3DRA was not significantly different from that of corresponding 2D-DSA ($p = 0.48$). A detailed representation of radiation dose output from the 3DRA acquisitions is shown in Table 3 and a comparative analysis in Fig. 1.

In all examinations, there was excellent depiction of relevant vascular anatomy by the 3DRA-CT images. MRI fusion allowed precise neuroanatomical relationships to be demonstrated. Some representative scenarios that 3DRA-CT and MRI fusion are additionally helpful are described below.

1. Localizing the nidus of small AVMs.

The exact neuroanatomical location of small AVM niduses can be challenging to determine but is critical to evaluate treatment options. This is more so for deep niduses (Fig. 2). Similarly, localization of a recurrent AVM nidus after treatment can be challenging on MRI or CT

Table 3 Radiation dose comparison for 3DRA examinations grouped according to protocol, vessel, and relative contribution to the radiation dose for the examination

3DRA Protocol	Mean $K_{a,r}$ (mGy) [Range]			Radiation dose comparison [Range]		
	3DRA acquisition	Biplane DSA acquisition ^a	Total examination ^b	3DRA vs. Biplane DSA acquisition	3DRA vs. Normalized (10-s) biplane acquisition ^c	3DRA vs. total examination
5-s 3DRA Subtracted (<i>N</i> = 11)	46.4 [21.5–66.5]	46.2 [18.3–109.4]	639.6 [51.5–1689.7]	132.2% [51.7–309.5]	148.9% [76.4–391.4]	12.5% [3.3–41.8]
5-s 3DRA Unsubtracted (<i>N</i> = 7)	2.6 [2.3–3.1]	49.6 [27.9–69.7]	332.8 [75.9–688.8]	5.9% [3.3–8.4]	7.0% [3.9–11.7]	1.2% [0.4–3.1]

$K_{a,r}$ Reference point air kerma

^a Standard anteroposterior and lateral DSA acquisition in the same artery

^b Including 3DRA, fluorography, and fluoroscopy

^c 10-s biplane DSA acquisition

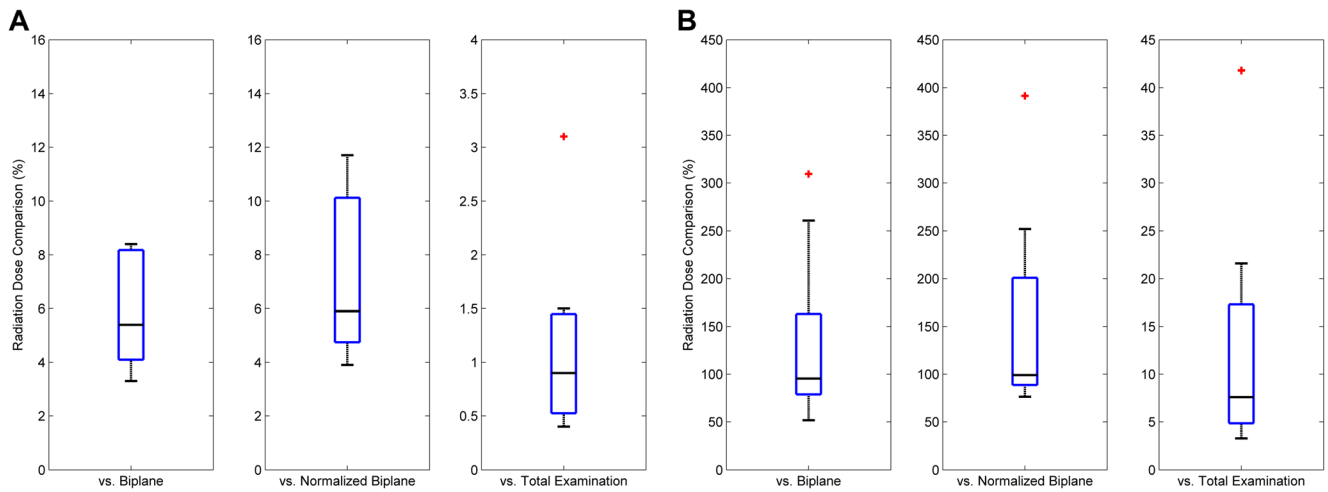


Fig. 1 Box-and-whisker plots depicting the comparative radiation dose ($K_{a,r}$) of 3DRA acquisition **a** without subtraction and **b** with subtraction. The three plots represent a comparison against standard 2D-DSA in the same vessel, normalized (10-s) 2D-DSA acquisition, and the total

examination. *Boxes* denote median, lower, and upper quartiles, with *whiskers* capturing values outside the interquartile range. Outliers are indicated in *red* and extend to values greater than 1.5 times the interquartile range

due to postoperative changes, embolic material, and non-specific enhancement. MRI fusion of 3DRA-CT can provide a definite answer (Fig. 3), leading to increased confidence in treatment decisions.

2. Characterizing angioarchitecture of AVMs.

Determining the presence, location, and access to an intranidal aneurysm can be difficult in compact nidus AVMs. In this setting, 3DRA-CT allows for better

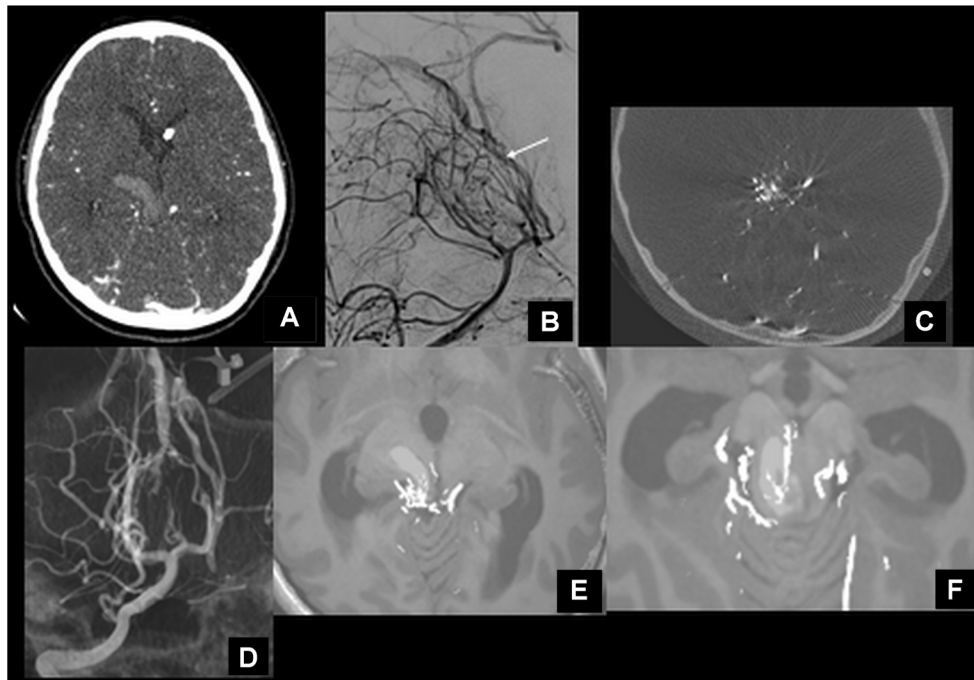


Fig. 2 Nine-year-old girl who presented acutely with brainstem hemorrhage. **a** CT angiography performed at admission showing acute right thalamic hemorrhage with no abnormal vessels noted. A left-sided ventricular drain is in place. **b** Right vertebral artery injection during subsequent DSA showing an indefinite mesencephalic blush supplied by thalamoperforators and a prominent left collicular artery (*arrow*). Fistulous communication into the Galenic venous system is seen. **c** 3DRA-CT from unsubtracted 3DRA in the right vertebral artery with

30% contrast shows a vascular nidus at the posterosuperior aspect of the hematoma. **d** Thick MIP image from 3DRA-CT, showing feeders from bilateral posterior cerebral arteries. **e, f** Fusion of axial MIP 3DRA-CT images with non-contrast 3D-T1 MRI, demonstrating the AVM nidus overlying the right superior colliculus and medial geniculate body. Arterial feeders from the right PCA and midbrain perforators are delineated, as are feeders from the P3 segment of the left PCA

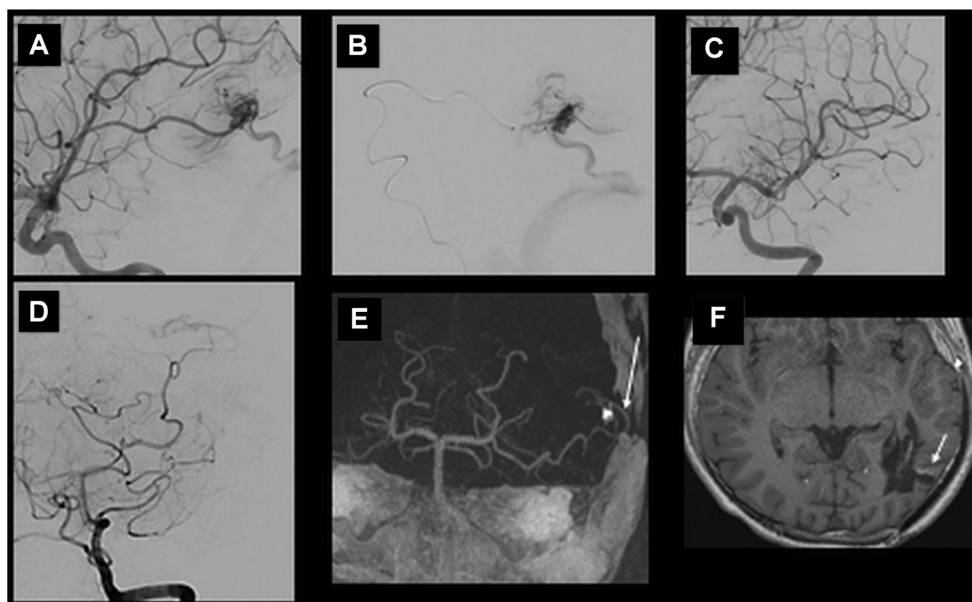


Fig. 3 Ten-year-old male who presented with acute posterior temporal hemorrhage from AVM rupture. **a** Compact nidus AVM supplied by the temporo-occipital branch of the left middle cerebral artery. **b** Microcatheter injection prior to embolization with 40% *N*-butyl cyanoacrylate glue in lipiodol. **c** Follow-up angiogram after 3 months with no filling of the nidus on left internal carotid injection. There was also no filling from vertebral injection (not shown here). **d** Follow-up

angiogram after 1-year shows recurrence from a lateral inferior temporal branch of the left posterior cerebral artery. **e** Thick MIP image from the 3DRA-CT (unsubtracted 3DRA with 30% contrast) showing the feeder, nidus postero-superior to the glue cast, and the cortical draining vein (*arrow*). **f** Fusion with non-contrast 3D-T1 MRI depicting the nidus (*arrow*) on the surface of the hemorrhagic cavity. Given the location of the nidus and draining vein, the lesion was considered most amenable for surgery

assessment of AVM angioarchitecture and relevant neuroanatomy (Fig. 4) crucial for endovascular treatment planning. For example, multiple feeding arteries can be traced without the venous contamination inherent to CTA, and nidus-associated aneurysms can be accurately delineated at multiple projections. Further, the absence of venous contamination in 3DRA-CT is beneficial in depicting sites of intranidal fistulae.

3. Depicting anatomy.

3DRA-CT can prove beneficial to delineate abnormal or variant anatomy (Fig. 5), when relevant for making therapeutic decisions. Multiplanar visualization allows for a better understanding of the neurovascular anatomy and is also useful for discussion with neurosurgeons. The

origin and course of small arteries can be determined for increased efficiency during interventional treatments. The usefulness of this has been demonstrated in the adult literature in cases of dural AVF [15] and for head and neck tumor embolization [16].

4. Distinguishing infundibulae from small aneurysms.

Distinguishing infundibulae from small aneurysms is challenging, and more so in children, when technical execution of MRA and CTA is often suboptimal. In addition, pediatric CTA presents additional complications with respect to aggressive radiation dose reduction, non-isotropic voxels, and partial voluming effects. 3DRA-CT is very useful in this regard, particularly in the presence of distorted anatomy (Fig. 6).

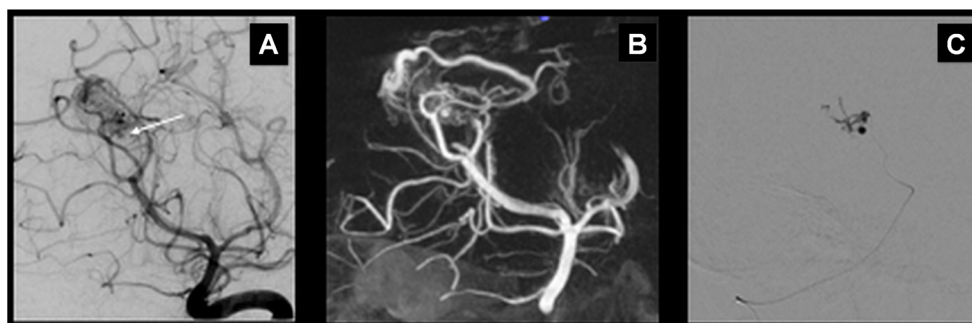


Fig. 4 Seven-year-old female with intraventricular hemorrhage from a ruptured AVM. **a** Left vertebral angiography showing a right choroidal AVM, with a tiny intranidal aneurysm (*arrow*). **b** 3DRA-CT from unsubtracted 3DRA with 30% contrast in left vertebral artery,

reformatted into oblique MIP image, clearly delineates the intranidal angioanatomy including the aneurysm and draining vein. **c** 33% *N*-butyl cyanoacrylate glue injection showing filling of the intranidal aneurysm and contiguous nidus

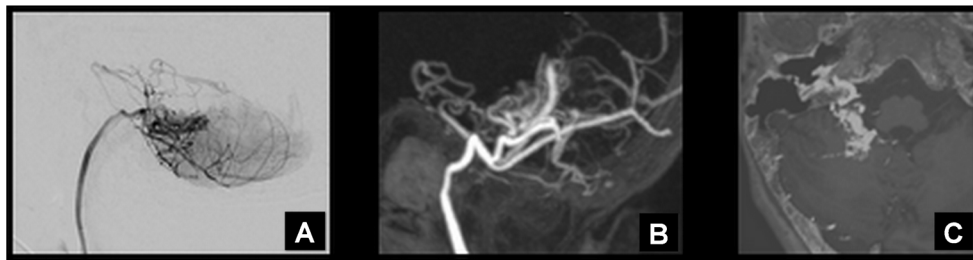


Fig. 5 Eleven-year-old male with variant posterior fossa vascular anatomy. **a** Catheter angiogram showing a cerebellar AVM fed by the right ascending pharyngeal artery, which constitutes the post-choroidal lateral branch of the right posterior inferior cerebellar artery. **b** Anatomy depicted on thick MIP reformat from 3DRA-CT from unsubtracted

3DRA with 30% contrast in the ascending pharyngeal artery. Prominent cerebellar vessels represent venous congestion, also seen on DSA. **c** Axial MRI fusion image showing the course of the neuromeningeal trunk through the jugular foramen supplying a subpial AVM of the right flocculus

Discussion

2D-DSA is the current gold standard for evaluating complex neurovascular lesions. The dynamic nature of the examination and excellent spatial resolution allow targeted assessment of cerebrovascular pathology including small aneurysms, feeders to shunting lesions, and collateral pathways in the head and neck. The ability of most new biplane flat-panel systems to perform a tomographic acquisition enables angiography to be

performed with isotropic datasets generated. Whereas 3DRA images are traditionally volume rendered for analysis, the ability to reconstruct this data into CT-like sections is not widely utilized. Axial CT sections generated can be visualized as such, or reformatted into VR, MIP, and oblique MPR images to precisely delineate cerebrovascular anatomy. This technique combines the high spatial resolution of DSA with the multiplanar reformatting capability of CT. Furthermore, unlike traditional CTA, the information derived in 3DRA-CT is

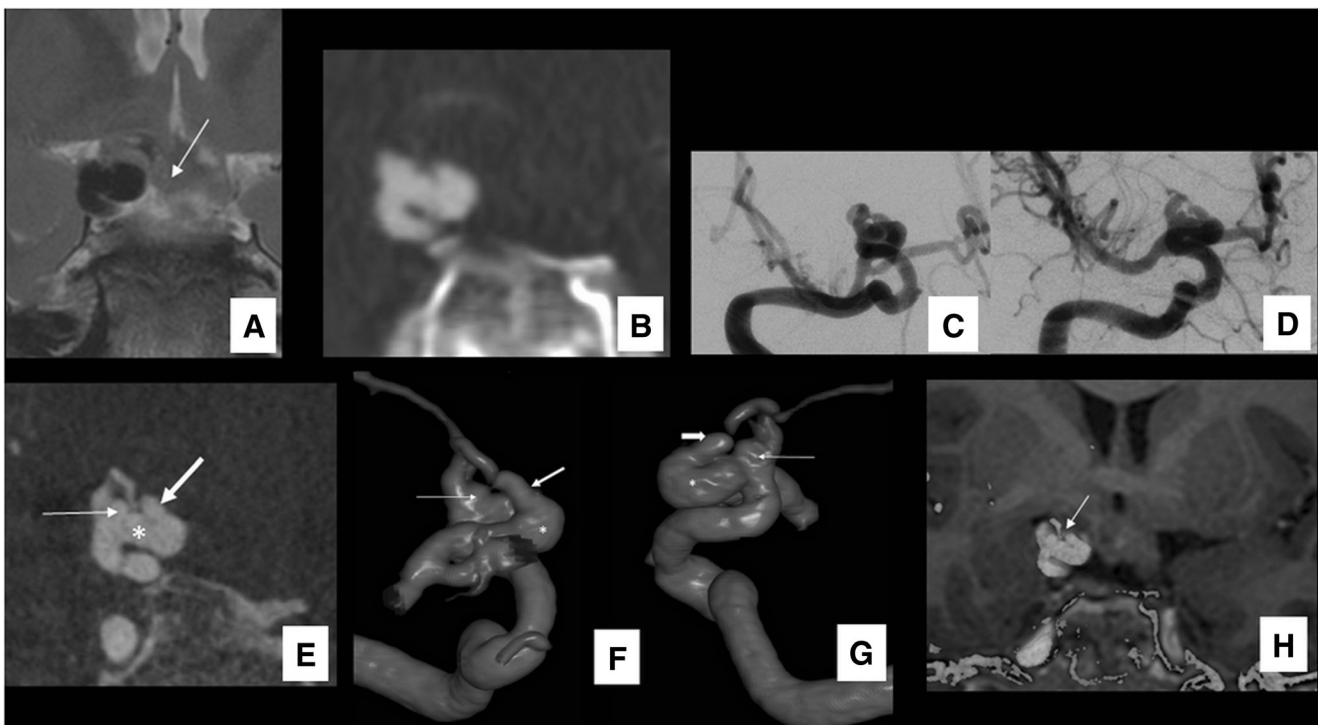


Fig. 6 Nine-year-old male with sellar-suprasellar tumor and right internal carotid artery aneurysm. **a** Coronal T2 MRI image shows the solid-cystic tumor (*arrow*) and suspicion for medially directed right internal carotid artery aneurysm. **b** Coronal MIP image from conventional CTA shows an ectatic arterial segment. **c, d** DSA images in **c** oblique and **d** anteroposterior projections showing the ectatic post-communicating segment, small posterior communicating aneurysm, and infundibular origin of the anterior choroidal artery. **e** Coronal image from 3DRA-CT (unsubtracted 3DRA in the right internal carotid artery with 30% contrast) showing the ectatic segment with a

wide-necked posterior communicating aneurysm (*thin arrow*) and anterior choroidal ostial infundibulum (*thick arrow*). **f, g** Volume-rendered images from 3DRA-CT showing the same anatomy. The tortuous communicating segment loop (*asterisk*), posterior communicating aneurysm (*thin arrow*), and infundibular origin of the anterior choroidal artery (*thick arrow*) are clearly defined. **h** Coronal reformatted fusion image MIP 3DRA-CT image with non-contrast 3D-T1 MRI, showing the cause of the infundibular appearance of the anterior choroidal ostium to be due to impression by the tumor (*arrow*)

from a selective arterial injection in the vessel of interest. CTA images are plagued by contrast contamination across vascular phases, resulting in difficult arteriographic post-processing. This is also true for long duration (20 s) CBCTA examinations, which can result in artifacts from motion and reduced clarity [17]. However, as we have shown, excellent CT-like image quality can be obtained from 5-s 3DRA acquisitions, at radiation dose levels far lower than biplane fluorography, while retaining optimal spatial resolution and minimizing artifact from motion and venous contamination.

In the adult neuroangiographic literature, CBCT has proven to be a useful adjunct tool in delineation of dural arteriovenous fistulas [3, 18], allowing submillimeter analysis of fistulae, arterial feeders, and draining veins and for detecting stent strut apposition to arterial walls [5–7]. In children, where vessels and lesions are typically smaller, we have shown that 5s-3DRA-CT and MRI fusion can prove advantageous with a reduced radiation burden. The short acquisition time allows a higher contrast flow rate to be employed, permitting adequate filling of distal arterial branches and aneurysms, small feeders to shunts, as well as better visualization of collateral anastomoses. Another important advantage of 5-s over 20-s CBCT, especially relevant in children, is the significantly reduced radiation dose, which has been reported to be more than 10 times less [19, 20]. Recently, 8-s CBCT was shown to have a lower effective radiation dose than standard biplane angiography in adults [21]. From our pediatric data, the radiation dose of a 5s-3DRA acquisition ranged from <4% to >300% that of a standard biplane acquisition, depending on technical factors (use of a separate mask run, copper filtration, etc.) and clinical factors (size of patient, duration of acquisition, etc.). However, with a customized unsubtracted 3DRA protocol utilizing higher kVp, heavy copper filtration, and reduced dose/pulse, the relative radiation burden was negligible, with a mean output being 5.9% (range 3.3–8.4%) of a comparable biplane acquisition. Similarly, when compared to the radiation from the entire examination, the radiation contribution of this unsubtracted 3DRA protocol was a mean of 1.2% (range 0.4–3.1%). As expected, subtracted 3DRA protocols, employing a second non-contrast masking acquisition, and using less aggressive dose reduction protocols, delivered greater radiation dose than their unsubtracted counterparts. When compared to biplane 2D-DSA, the $K_{a,r}$ for subtracted 3DRA ranged from 52 to 310% (mean = 132%) and 3.3–42% (mean = 12.5%) of the total procedure. The procedure accounting for 42% of the total examination dose was a single vessel check examination for previously treated AVM, with a low total $K_{a,r}$.

There are inherent differences between 3DRA with and without subtraction, which direct the clinical scenarios where each might be useful. Table 2 summarizes the advantages and disadvantages of each of these protocols for clinical situations. The operator can choose one, depending on the clinical scenario, additional information required, and type of post-processing planned. In our practice, we perform 3DRA without subtraction

when more information can be obtained from CT reconstruction and MRI fusion than from VR representation. We perform subtracted 3DRA when working projections are required during neurointerventional procedures. However, although the radiation cost is greater, 3DRA with subtraction remains an important technique when evaluating lesions near bony structures (e.g., the skull base) or in the presence of previous embolic material. In several instances, however, subtraction is not required and complete diagnostic information can be obtained with adequate post-processing of an unsubtracted 3DRA acquisition. Therefore, even when multiple projection views are required, we default to 3DRA without subtraction, given the significantly lower radiation dose, and post-process 3DRA-CT with thick MIP images instead of VR reformats. Considering the enhanced processing capabilities opened up by 3DRA, multiple 2D-DSA projections can often be avoided, resulting in further reduced radiation dose to the patient. Our practice of diluting the contrast to 30% for unsubtracted 3DRA acquisition, primarily to reduce streak artifact from beam hardening, also reduces contrast volume. Future work will investigate similar technical customization for the subtracted 3DRA protocols as have been implemented for the unsubtracted 3DRA protocols. The reconstruction and calculation of procedure, protocol, and application-specific effective dose for pediatric neuroangiographic 3DRA are also an objective to be pursued.

Although these comparisons relate to the practice at this institution in addition to the technical factors of our implemented biplane DSA protocols, the ability to acquire and reconstruct diagnostic 3DRA-CT at a minimal radiation cost was a significant outcome of this work. The technique is inherently more effective in children, the majority of catheter angiograms being performed under general anesthesia. There is a tendency to avoid performing 3DRA in children, performing instead several oblique 2D-DSA acquisitions, in situations where further information is required. In our pediatric cohort, the radiation dose of subtracted 3DRA in children was comparable to that of a standard biplane acquisition, while for unsubtracted 3DRA it was 12 to 30 times less than a standard biplane acquisition. Therefore, when there is substantial clinically relevant information to be obtained from a 3DRA volume acquisition, these above findings may be included in the benefit/risk analysis of performing such an acquisition. Although we did not prospectively evaluate the potential reduction in number of DSA acquisitions from performing 3DRA, the increased post-processing capabilities and multiplanar viewing often resulted in the operator not acquiring multiple oblique and magnified images. In the adult literature too, 3DRA has been shown to significantly reduce the number of DSA exposures [22].

Most children have a brain MRI as the initial diagnostic step prior to catheter angiography. Through our examples, we have demonstrated how MRI fusion of 3DRA-CT adds another level to the diagnostic capability of modern angiographic systems. Precise angio-topographical localization is crucial

for diagnosis as well as endovascular or neurosurgical treatment planning in complex lesions like AVMs and pial AVFs. The soft tissue resolution of MRI added to the spatial and temporal resolution of DSA allows neurovascular anatomy and neuroanatomical relations of lesions to be clearly defined. This allows for increased confidence in devising treatment strategies, for example by MRI localization of recurrent AVM nidus as defined by catheter angiography for presurgical planning and neuronavigation.

Conclusion

3DRA-CT and fusion with MRI are useful tools in the evaluation and treatment of complex cerebrovascular lesions in the pediatric population. These techniques provide a unique ability to examine angioarchitecture and neurovascular relations for treatment planning while reducing the total radiation dose and contrast volume of the study.

Compliance with ethical standards

Funding No funding was received for this study.

Conflict of interest The authors declare that they have no conflict of interest.

Ethical approval All procedures performed in the studies involving human participants were in accordance with the ethical standards of the institutional Research Ethics Board (REB) with REB#1000 055502 and with the 1964 Helsinki Declaration and its later amendments or comparable ethical standards. For this type of study formal consent is not required.

Informed consent Informed consent was obtained from all individual participants included in the study.

References

- Honarmand AR, Gemmete JJ, Hurley MC, Shaibani A, Chaudhary N, Pandey AS et al (2015) Adjunctive value of intra-arterial cone beam CT angiography relative to DSA in the evaluation of cranial and spinal arteriovenous fistulas. *J Neuro Intervent Surg* 7(7): 517–523
- Safain MG, Rahal JP, Patel S, Lauric A, Feldmann E, Malek AM (2014) Superior performance of cone-beam CT angiography in characterization of intracranial atherosclerosis. *J Neurosurg* 121(2):441–449
- Eesa M, Sharma P, Mitha AP, Sutherland GR, Goyal M (2009) Angiographic computed tomography with selective microcatheterization in delineating surgical anatomy in the case of a dural arteriovenous fistula. *Technical note J Neurosurg* 111(5):916–918
- Schulz CJ, Schmitt M, Böckler D, Geisbüsch P (2016) Intraoperative contrast-enhanced cone beam computed tomography to assess technical success during endovascular aneurysm repair. *J Vasc Surg* 64(3):577–584
- Patel NV, Gounis MJ, Wakhloo AK, Noordhoek N, Blijd J, Babic D et al (2011) Contrast-enhanced angiographic cone-beam CT of cerebrovascular stents: experimental optimization and clinical application. *AJNR Am J Neuroradiol* 32(1):137–144
- Clarençon F, Piotin M, Pistorocchi S, Babic D, Blanc R (2012) Evaluation of stent visibility by flat panel detector CT in patients treated for intracranial aneurysms. *Neuroradiology* 54(10):1121–1125
- Heran NS, Song JK, Namba K, Smith W, Niimi Y, Berenstein A (2006) The utility of Dyna CT in neuroendovascular procedures. *Am J Neuroradiol* 27(2):330–332
- Shinohara Y, Sakamoto M, Takeuchi H, Uno T, Watanabe T, Kaminou T et al (2013) Subarachnoid hyperattenuation on flat panel detector-based conebeam CT immediately after uneventful coil embolization of unruptured intracranial aneurysms. *AJNR Am J Neuroradiol* 34(3):577–582
- Orth RC, Wallace MJ, Kuo MD (2009) C-arm cone-beam CT: general principles and technical considerations for use in interventional radiology. *J Vasc Interv Radiol* 20(7):S538–S544
- Bai M, Liu B, Mu H, Liu X, Jiang Y (2012) The comparison of radiation dose between C-arm flat-detector CT (Dyna CT) and multi-slice CT (MSCT): a phantom study. *Eur J Radiol* 81(11):3577–3580
- van Rooij WJ, Sprengers ME, de Gast AN, Peluso JPP, Sluzewski M (2008) 3D rotational angiography: the new gold standard in the detection of additional intracranial aneurysms. *Am J Neuroradiol* 29(5):976–979
- Bechan RS, van Rooij SB, Sprengers ME, Peluso JP, Sluzewski M, Majoie CB et al (2015) CT angiography versus 3D rotational angiography in patients with subarachnoid hemorrhage. *Neuroradiology* 57(12):1239–1246
- Shi W-Y, Li Y-D, Li M-H, Gu B-X, Chen S-W, Wang W et al (2010) 3D rotational angiography with volume rendering: the utility in the detection of intracranial aneurysms. *Neurol India* 58(6):908–913
- Ruijters D, Homan R, Mielekamp P, van de Haar P, Babic D (2011) Validation of 3D multimodality roadmapping in interventional neuroradiology. *Phys Med Biol* 56(16):5335–5354
- Hui T, Kitagawa N, Morikawa M, Hayashi K, Horie N, Morofuji Y et al (2009) Efficacy of Dyna CT digital angiography in the detection of the fistulous point of dural arteriovenous fistulas. *Am J Neuroradiol* 30(3):487–491
- Kakeda S, Korogi Y, Miyaguni Y, Moriya J, Ohnari N, Oda N et al (2007) A cone-beam volume CT using a 3D angiography system with a flat panel detector of direct conversion type: usefulness for superselective intra-arterial chemotherapy for head and neck tumors. *Am J Neuroradiol* 28(9):1783–1788
- Nagarajappa AK, Dwivedi N, Tiwari R (2015) Artifacts: the downturn of CBCT image. *J Int Soc Prev Community Dent* 5(6):440–445
- Aadland TD, Thielen KR, Kaufmann TJ, Morris JM, Lanzino G, Kallmes DF et al (2010) 3D C—arm conebeam CT angiography as an adjunct in the precise anatomic characterization of spinal dural arteriovenous fistulas. *Am J Neuroradiol* 31(3):476–480
- Wang C, Nguyen G, Toncheva G, Jiang X, Ferrell A, Smith T et al (2014) Evaluation of patient effective dose of neurovascular imaging protocols for C-arm cone-beam CT. *AJR Am J Roentgenol* 202(5):1072–1077
- Seguchi S, Saijou T, Ishikawa Y, Koyama S (2014) Radiation dose evaluation in 3D rotation angiography and cone-beam computed tomography with a flat panel detector. *Nihon Hōshasen Gijyutsu Gakkai Zasshi* 70(7):646–652
- Guberina N, Lechel U, Forsting M, Mönninghoff C, Dietrich U, Ringelstein A (2016) Dose comparison of classical 2-plane DSA and 3D rotational angiography for the assessment of intracranial aneurysms. *Neuroradiology* 12
- Abe T, Hirohata M, Tanaka N, Uchiyama Y, Kojima K, Fujimoto K et al (2002) Clinical benefits of rotational 3D angiography in endovascular treatment of ruptured cerebral aneurysm. *AJNR Am J Neuroradiol* 23(4):686–688